Electro-optic hybrid aligned nematic device utilizing carbon nanotube arrays and two-dimensional hexagonal boron nitride nanosheet as alignment substrates

Rajratan Basu and Derek T. Gess

Phys. Rev. E **104**, 054702 — Published 29 November 2021

DOI: 10.1103/PhysRevE.104.054702

Electro-optic HAN device utilizing carbon nanotube arrays and 2D hexagonal boron nitride nanosheet as alignment substrates

Rajratan Basu* and Derek T. Gess

Department of Physics, Soft Matter and Nanomaterials Laboratory, The United States Naval Academy, Annapolis, MD 21402, USA.

Hybrid-aligned nematic (HAN) liquid crystal (LC) devices have both fundamental and technological importance for their applications in LC adaptive lenses, low voltage LC displays, smart windows, and many more. We report the fabrication and characterization of a novel nanostructure-based HAN device employing vertically aligned carbon nanotube (VA-CNT) arrays as the homeotropic alignment agent on one side and 2D hexagonal boron nitride (*h*-BN) as the planar alignment agent on the other side of the LC cell. The LC achieves the HAN configuration in the cell, *i.e.*, homeotropic alignment at the VA-CNT side due to the π-π stacking interaction between the LC and CNTs, and planar alignment at the *h*-BN side due to the π-π stacking interaction between the LC and *h*-BN. When an applied electric field is ramped up across this VA-CNT/*h*-BN HAN cell, the LC (positive anisotropic) obtains a homeotropic state, requiring no threshold voltage to start the reorientation process—this effect is similar to that of a traditional polyimide (PI)-based HAN device. This VA-CNT/*h*-BN HAN cell successfully demonstrates the optical, electro-optical operations and the electric field-induced dynamic response. This study reveals that two inorganic nanostructured surfaces, *i.e.*, VA-CNT arrays and 2D *h*-BN, can efficiently replace the *organic* PI alignment agents when needed and retain the HAN device's necessary electro-optical performances. These results substantially expand the fundamental understanding and the scope of utilizing various nanostructured surfaces for LC alignment mechanisms.

*Electronic address: basu@usna.edu

I. INTRODUCTION

Electro-optic liquid crystal (LC) devices are essential in modern display applications, and realizing various LC—substrates interactions is still a fundamental area of research. The LC displays (LCDs) utilize a variety of electro-optic LC cells, such as homogeneous planar cells, homeotropic cells, twisted-nematic cells, in-plane switching cells, and hybrid-aligned nematic (HAN) cells. A HAN device is unique in its class because it can employ both positive and negative dielectric anisotropic LCs for the electro-optic operation, and unlike planar or homeotropic LC cells, a HAN cell needs no threshold voltage for the onset of an electro-optic response [1,2]. In a HAN cell, LC molecules obtain homeotropic alignment at one boundary surface and homogeneous planar alignment at the other [1]. This HAN configuration is important in both fundamental and applied research areas. For example, the flexoelectric polarization is a fundamental property of a nematic LC; and a strong splay-bend deformation is generated in the HAN state on account of the asymmetry in the molecular distribution—which is convenient for measuring the flexoelectric polarization of a nematic LC [3,4,5]. In the applied direction, the electro-optic HAN devices are utilized for low operating voltage LCDs [1], zenithal bistable devices [6], smart windows [7], high-speed switching LCDs [8], dual-operation-mode LC lenses [9], and polarization rotators [10].

Generally, various polyimide (PI) layers are used as the planar alignment and vertical alignment agents in traditional HAN devices [11]. The commonly used planar-alignment agent is a unidirectionally rubbed PI (*e.g.*, Nissan SE-6414, KPI-300B, etc.)-coated surface. The LC molecules align with the alkyl side chains of the PI substrate along the rubbing direction and form a uniform planar director profile on the PI substrate [12]. On the other hand, for homeotropic alignment, LC molecules align with the vertical part of the alkyl side chains of a PI substrate (*e.g.*, Nissan SE-4811, DPI-V011, etc.).

Even though these *organic* PI alignment agents are widely used in LCDs, they have some limitations. For example, the PI layers, being organic materials, are receptive to UV rays and extreme temperatures. Therefore, the alignment qualities can be altered when the PI-based LC devices are exposed to UV light and high temperatures [13,14]. In addition, the conventional rubbing process of the PI has some disadvantages as well. The temperature variation during the rubbing process of the PI substrate significantly impacts the LC alignment mechanisms [15]. The LC can be contaminated from the occurrence of fiber dust particles from the rubbing process of

the PI [11]. A non-uniform brightness in the LCD panel can be triggered by a wide distribution of pre-tilt angles resulted from an uneven rubbing process [11]. Ion impurities can stem from the PI alignment layers into the LC [16]. Therefore, studying LC alignment mechanisms on various substrates and finding alternative alignment substrates is an important area of fundamental research—which has potential applications in designing novel electro-optic LC devices.

Inorganic nanostructured surfaces are generally not responsive to UV rays and high temperatures. Therefore, a variety of inorganic nanostructured alignment agents have recently been explored in electro-optic LC devices to address the PI alignment agent-related issues [14,17,18,19,20,21,22,23,24,25,26,27,28].

This work studied the LC alignment on two inorganic nanostructured surfaces: vertically aligned carbon nanotube (VA-CNT) arrays and two-dimensional (2D) hexagonal boron nitride (*h*-BN), and then employed them as the homeotropic alignment agent and the planar alignment agent, respectively, to design a novel nanostructure-based electro-optic HAN device. We present that this inorganic nanostructured alignment agents-based HAN cell maintains its electro-optic performances like a traditional PI-based HAN cell.

II. EXPERIMENTS, RESULTS, AND DISCUSSION

This section presents the interactions of the LC with VA-CNTs and *h*-BN, the fabrication of the VA-CNT/*h*-BN-based HAN cell, the electro-optical effect of the LC in the cell, and the dynamic electro-optic switching response of the cell.

A. Fabrication of the VA-CNT/h-BN-based HAN cell

We have commercially used a plasma-enhanced chemical vapor deposition (PECVD) system at NanoLab, Inc. [29] in Waltham, Massachusetts, USA, to produce the VA-CNT arrays. Several quartz substrates (2.5 × 2.5 cm^2) were first coated with a chromium (Cr) adhesion layer (2 nm). The Cr-coated quartz substrates were overcoated with nickel nanoparticles for the growth of the VA-CNT arrays. The freestanding CNTs grew vertically from the substrate surface in the PECVD system. The CNT length was controlled by the processing time, and the diameter was controlled by the nickel particle size. Therefore, each CNT-tip was capped with a nickel nanoparticle. These

VA-CNTs had multilayer graphitic sidewalls and a hollow core. The experimental procedure of the PECVD grown VA-CNT arrays is given elsewhere in detail [30]. The PECVD system was adjusted to grow the VA-CNT arrays with a CNT site density of ~ 10^8 cm^{-2}, an average length of ~ 1.5 μm, and an average diameter of ~ 70 nm. Figs. 1(a) and (b) show the scanning electron microscope (SEM) images of the top-view of the VA-CNT arrays. The inset in Fig. 1(b) shows the side view of the arrays. This method produced the CNT arrays that are tilted a little (~2^o) from the vertical direction. See the inset in Fig. 1(b). Please note that this 2^o tilt angle is an average estimate. Using an SEM image, we measured the angle of deviation from the verticle direction for 100 random CNTs separately by an image processing software, and the average value of those 100 angles was approximately 2^o.

It is known that the LC molecules bind to the CNT walls due to a non-covalent interaction enhanced by the π-π stacking [31] between the LC's benzene rings and the CNT's honeycomb structure, as schematically shown in Fig. 1(c). The binding energy associated with π-π stacking interaction is ~ 2.0 eV/molecule [31]. This strong interaction between the LC and the CNT gives rise to several scientifically important and fascinating phenomena. For example, this interaction results in self-assembly of the CNTs along the nematic director in an LC-CNTs colloidal suspension, and the LC molecules orient along the CNT-long axis at the CNT-surface [32,33,34,35]. Other phenomena in various LC-CNTs colloidal suspensions include the formation of pseudo-nematic domains surrounding the CNT-long axis in the isotropic phase [35,36], an increase in the nematic orientational order parameter [34], CNT induced chirality in otherwise achiral LCs [37,38,39,40,41], and a faster LC switching resulted from the enhancement of polar anchoring energy [42]. In the present work, the VA-CNT arrays and the LC-CNT interaction are exploited to achieve homeotropic alignment at one boundary surface of the HAN cell. Figure 1(c) illustrates a VA-CNT-assisted homeotropic LC alignment. We first coated a VA-CNT slide with a thin layer LC E7 (T_{NI} = 60.5 ^{o}C, *EMD Millipore Corporation*) by putting a small LC droplet and then gently blowing it away by a dust blower—which left a sufficiently thin LC film on the substrate. We then studied the LC alignment on the VA-CNT slide under an optical microscope (Olympus BX61). Figure 1(d) shows both an LC-covered VA-CNTs region and a bare VA-CNTs region. Figure 1(e) shows an entire region of LC-covered VA-CNTs. Both Figs. 1(d) and 1(e) were taken using parallel-polarized light. When cross-polarized light was used, the LC texture turned completely dark, as shown in Fig. 1(f); and the texture remained dark as the slide was

rotated under the cross-polarized microscope—this proves that the VA-CNT arrays promote homeotropic alignment of the LC. An *unaligned* LC texture on a bare glass substrate (without the VA-CNTs) under the cross-polarized microscope is shown in the inset in Fig. 1(f) for comparison.

On the other hand, the 2D *h*-BN nanostructure is known to induce planar alignment [20,21,22,43] to the LC molecules due to the epitaxial (π-π stacking) interaction between the LC and the *h*-BN lattice—which is illustrated by overlaying of the LC's benzene rings on the *h*-BN-honeycomb structure in Fig. 2(a). First, the chemical vapor deposition (CVD) grown monolayer *h*-BN film on a copper foil was obtained commercially from *Graphene Supermarket*, *Inc*. It is well documented that for a monolayer *h*-BN sheet, the Raman peak is ~ 1370 cm^{-1} [44]. Figure 2(b) shows the Raman spectroscopy of *h*-BN with a peak at ~ 1370 cm^{-1} confirming the presence of the monolayer *h*-BN on the copper foil. The monolayer *h*-BN film was then transferred from the copper foil onto several 2.5 × 2.5 cm^2 ITO coated glass substrates using the standard polymethyl-methacrylate (PMMA) assisted wet transfer method [45,46]. To realize the LC alignment on the *h*-BN film, a thin LC E7 layer on the *h*-BN slide was formed by putting a small LC droplet and then gently blowing it away by a dust blower. The LC layer on the *h*-BN slide was heated up into the isotropic phase and cooled down into the nematic phase in a cyclic manner to remove any remaining order resulted from the coating process. The cross-polarized optical microscope was used to study the alignment of the LC on the *h*-BN film on the ITO slide. The microphotograph in Fig. 2(c) shows a bright uniform LC texture under the cross-polarized microscope where the LC director $\hat{n}$ is at 45° with the crossed polarizers. A dark uniform LC texture is achieved in Fig. 2(d) when $\hat{n}$ is parallel to the analyzer. This verifies that the LC molecules achieve planar alignment on the *h*-BN lattice. The multiple lines and spots observed in Figs. 2(c) and (d) are from the PMMA residues from the transfer process. Note that the LC molecules can assume three different alignment directions separated by 60° on an *h*-BN nanosheet due to the hexagonal symmetry similar to that of a graphene layer [19]. This alignment degeneracy is discussed elsewhere in detail [19]. However, even with this three-fold alignment degeneracy, it is still possible to get reasonably large LC domains (> 0.5 × 0.5 mm^2) with unidirectional planar alignment on the *h*-BN. This can be seen in Figs. 2(c) and (d)—which show a single domain with uniform intensity. This unidirectional domain size is large enough for our experiment. From the application point of view, in modern high-resolution LCDs, the typical pixel width is ~250 μm or

less. Therefore, it could be possible to employ the *h*-BN nanosheet as the planar-alignment agent in individual pixels as long as a uniform domain size is more than a pixel's dimension in the LCD.

Before making the HAN cell, the optical transmission spectra through a standard PI on ITO coated *glass* slide, the monolayer *h*-BN on ITO coated *glass* slide, and the VA-CNT arrays on Cr coated *quartz* slide were studied for comparison purposes. The optical transmission spectra were measured for the three slides separately using a FLAME-S-XR1-ES spectrometer (*Ocean Optics, Inc.*) and DH-2000-BAL UV-VIS-NIR light source (*Ocean Optics, Inc.*). The transmission spectra for these slides in the wavelength range from UV to near IR are shown in Fig. 3. The *h*-BN/ITO slide revealed more optical transmission than the standard PI/ITO slide as monolayer 2D materials generally have high optical transparency. However, the VA-CNT/Cr slide showed smaller transmission than the other two slides because of the higher absorption of the CNTs along the vertical direction. Nonetheless, the optical transmission for the VA-CNT/Cr slide is still strong enough (in between ~ 60% to 75%) for utilizing in LC cells. Note that the origin of the onset of the strong absorption at 300-350 nm for the PI/ITO slide and the *h*-BN/ITO slide is from the glass substrates. Quartz substrates and glass substrates have different transmission spectra.

In our experiment, we put together a VA-CNT slide and an *h*-BN slide to make a HAN cell with an average cell-gap, $d = 11.4\ \mu$m. This HAN device was filled with LC E7 by capillary action from one opening and gentle vacuum suction from the other opening to support the average LC-flow in one direction during the LC filling process. The nematic LC director $\hat{n}$ obtained vertical alignment at the VA-CNT side and planar alignment at the *h*-BN side. This way, the LC achieved the HAN configuration in the cell—which is schematically shown in Fig. 4(a). Note that the slightly tilted CNT arrays helped the LC director in the HAN cell turn only in one direction, and consequently, the reverse director tilt degeneracy was eliminated in this HAN cell. Inside this cell, the LC showed a bright texture under the cross-polarized microscope when $\hat{n}$, at the *h*-BN side, was at 45^{o} with the crossed polarizers—see Fig. 4(b). As the cell was rotated by 45^{o}, $\hat{n}$, at the *h*-BN side, became parallel to the analyzer, and the LC revealed a completely dark texture, as shown in Fig. 4(c). We also commercially obtained traditional PI-based HAN cells ($d = 7\ \mu$m) from *Instec, Inc.*, for comparisons. A traditional PI-based HAN cell was filled with LC E7, and the textures for the two oriented states, 45^{o} and 0^{o}, are shown in Fig. 4(d) and Fig. 4(e), respectively. Both the VA-CNT/*h*-BN HAN cell and the traditional PI-based HAN cell showed similar LC

textures. For the VA-CNT/*h*-BN HAN cell, some dark patches can be seen in Fig. 4(b)—these are due to the PMMA residues from the *h*-BN transfer process. The black dots for the traditional PI-based HAN cell in Fig. 4(d) are the spacer particles.

It is known that thin Cr layers of thickness from 2 nm to 10 nm are highly transparent over a wide wavelength range and show high electrical conductivity [47]. Therefore, Cr layers (2 nm – 10 nm) can operate as high-quality transparent electrodes [47]. In the VA-CNTs production process, a Cr adhesion layer of 2 nm thickness was deposited on the glass slide for the growth of CNTs. This Cr adhesion layer was utilized as the transparent electrode on the VA-CNT side of the HAN cell. The Cr slide sheet resistance was ~ 1000 Ω/□ , and the Cr film thickness was 2 nm. As mentioned before, the *h*-BN nanosheet was transferred onto ITO slides, and the ITO was used as the transparent electrode on the *h*-BN side of the HAN cell. The ITO slide sheet resistance was ~ 20 Ω/□ , and the ITO film thickness was 160 nm.

B. Electro-optical effect of LC in the VA-CNT/h-BN HAN cell

In a traditional *planar aligned* LC cell, the electrically-controlled birefringence effect [48] is observed when the applied electric field across the cell exceeds its threshold value and the LC director $\hat{n}$ orients from the initial planar state to the final homeotropic state. This rotation of $\hat{n}$ results in a change in the LC's effective birefringence, $\langle \Delta n \rangle$ as a function of applied voltage. If $\hat{n}$ in a planar cell of cell-gap d is initially oriented at 45° with the crossed-polarizers, the intensity of the plane-polarized light (wavelength λ) incident on the LC cell is I_o, then the transmitted intensity I at the exit of the analyzer varies as [48]

$$I = I_O \sin^2\left(\frac{\pi d \langle \Delta n \rangle}{\lambda}\right) \tag{1}$$

As $\langle \Delta n \rangle$ changes during the rotation of $\hat{n}$ when the applied field is increased, a change in the optical phase difference, $\Delta\phi = \left(\frac{2\pi d \langle \Delta n \rangle}{\lambda}\right)$ results in an oscillatory optical signal at the exit of the analyzer. It is known that when $\hat{n}$ orients from the initial planar state to the final homeotropic state, the number of maxima that appears in the transmittance vs. voltage curve is given by $\left(\frac{d\,\Delta n}{\lambda}\right)$ [48].

A HAN cell at zero voltage has approximately *half* the effective birefringence of an unexcited planar cell [1]. Therefore, the zero voltage optical retardation in the HAN cell is approximately *half* of that in the planar cell for the same cell-gap [1]. When the electric field is applied across the HAN cell, the change in the phase difference from the HAN configuration to the homeotropic configuration is ~ $\frac{1}{2}\Delta\phi$ and, subsequently, the number of maxima that appears in the transmittance vs. voltage curve for the HAN cell is ~ $\frac{1}{2}\left(\frac{d\,\Delta n}{\lambda}\right)$.

The voltage-dependent transmittance experiment was conducted using an optical setup where the VA-CNT/*h*-BN HAN cell was mounted on a rotational stage between two crossed polarizers, and the LC director $\hat{n}$ at the planar side was oriented at 45^{o} with the crossed polarizers. A He-Ne laser beam of 5 mW power and 633 nm wavelength was sent through the polarizer, the VA-CNT/*h*-BN HAN cell, the crossed analyzer, and into a photodetector. A DC voltmeter was connected to the photodetector to measure the transmitted intensity. An applied AC voltage of frequency *f* =1000 Hz across the HAN cell was slowly ramped up from 0V to 20V, and the transmitted light signal captured by the photodetector was recorded from the DC voltmeter.

Figure 5 represents the electro-optical effect of the VA-CNT/*h*-BN HAN cell. Figure 5(a) exhibits the transmittance (I/I_o) curve as a function of the applied ac voltage. This curve clearly demonstrates that the LC did not need a threshold voltage for the onset of the electro-optic response in the VA-CNT/*h*-BN HAN cell. As discussed earlier, the number of maxima in the transmittance vs. voltage curve for a HAN cell is ~ $\frac{1}{2}\left(\frac{d\,\Delta n}{\lambda}\right)$. Using Δn = 0.225 for LC E7, λ = 633 nm for the He-Ne laser and, the VA-CNT/*h*-BN HAN cell-gap, d = 11.4 μm, we obtain $\frac{1}{2}\left(\frac{d\,\Delta n}{\lambda}\right) = 2$. The transmittance curve in Fig. 5(a) clearly shows *two* maxima. Together with the absence of a threshold voltage, this result of obtaining two maxima indicates that the LC indeed achieved the HAN configuration in the VA-CNT/*h*-BN cell. The zero-field HAN configuration and the high-field homeotropic configuration in the VA-CNT/*h*-BN cell are schematically illustrated in Fig. 5(b) and (c), respectively.

For comparison, a traditional PI-based HAN cell (d = 7 μm) and a traditional PI-based planar cell (d = 9 μm) from *Instec*, *Inc*. were also used to study the voltage-dependent transmittance effect

using LC E7. The top inset in Fig. 5(a) shows the transmittance vs. voltage curve for the PI-based HAN cell. This HAN cell shows the absence of a threshold voltage, like the VA-CNT/*h*-BN HAN cell. Using d = 7 μm, we obtain the number of maxima, $\frac{1}{2}\left(\frac{d\,\Delta n}{\lambda}\right) = 1.24$. Clearly, the PI-based HAN cell shows *one* complete maximum in the transmittance vs. voltage curve. The bottom inset in Fig. 5(a) shows the transmittance vs. voltage curve for the PI-based planar cell. This planar cell, as expected, shows a threshold voltage to start the reorientation process. Using d = 9 μm for this planar cell, we obtain the number of maxima, $\left(\frac{d\,\Delta n}{\lambda}\right) = 3.2,$ and the PI-based planar cell shows *three* complete maxima in the transmittance vs. voltage curve.

The same electro-optical effect experiment for the VA-CNT/*h*-BN HAN cell was also carried out under the cross-polarized microscope using a white light source. Several microphotographs of the cell at different applied voltages were taken, and seven such microphotographs are presented in Fig. 5(d) to show how the LC texture changed as the applied voltage was increased. Note that the transmittance intensities of the micrographs in Fig. 5 (d) do not directly correspond to the transmittance curve in Fig 5(a). The micrographs were taken under a white light source, and the transmittance curve was obtained using a red laser (*i.e.*, a monochromatic source).

C. Dynamic electro-optic switching response in the VA-CNT/*h*-BN HAN cell

The dynamic response is a critical concern for LC devices. Stable switching responses give a cell a better performance. The field-induced dynamic response in an LC cell is given by two characteristic times, τ_{on} (voltage on) and τ_{off} (voltage off) [48].

For an LC cell, the optical switching on, τ_{on} is defined by the time taken by the transmitted intensity to decay from 90% to 10% of its maximum value when the applied voltage is turned on. After the voltage is turned off, the transmitted intensity through the LC cell increases. The optical switching off, τ_{off} is the time taken by the transmitted intensity to rise from 10% to 90% of its maximum value. The same electro-optical setup was employed to study the dynamic response. In this case, the output of the photodetector was connected to a digital storage oscilloscope to record the change in transmitted intensity as a function of time when a 20 V square-wave voltage of 35 Hz was applied across the cell. The field-induced dynamic switching response is shown in Fig. 6. For the VA-CNT/*h*-BN HAN cell (d = 11.4 μm), we found that τ_{on} = 2.00 ms and τ_{off} = 7.20 ms

from Fig. 6(a). For comparison, this experiment was carried out for the traditional PI-based HAN cell (d = 7 μm) for the same applied voltage, and we found that τ_{on} = 0.90 ms and τ_{off} = 6.30 ms from Fig. 6(b). It is known that $\tau_{on/off} \propto d^2$ [48], therefore, the faster response for the PI-based HAN cell is attributed to its smaller cell-gap than the VA-CNT/*h*-BN HAN cell. When we calculate τ_{off}/d^2 (to eliminate the effect of the cell thickness) for both the cells, we obtain $(\tau_{off}/d^2)_{PI\ cell}$ = 0.128 ms/μm^2 and $(\tau_{off}/d^2)_{VA\text{-}CNT/h\text{-}BN\ cell}$ = 0.055 ms/μm^2. This indicates that a VA-CNT/*h*-BN HAN cell would show a faster τ_{off} than a PI HAN cell for the same cell thickness. Note that the bulk alignment of the LC in this nanostructured-based HAN cell is not different from that of the PI-based HAN cell. However, the LC/CNT and the LC/*h*-BN anchoring energy is much stronger (~2 eV/molecule) than the LC/PI anchoring energy. That is why the polar anchoring strength coefficient can increase significantly in the nanostructured-based LC cell [22].

If the backflow in the cell is neglected, τ_{off} is purely driven by the elastic interaction between the LC and the alignment substrates. Therefore, τ_{off} is greatly influenced by the polar anchoring strength coefficient [42,49]. It is also known that when the polar anchoring strength coefficient is significantly enhanced, τ_{off} is faster [42,50]. We believe that the polar anchoring strength coefficient is higher in the VA-CNT/*h*-BN HAN cell due to the strong LC/CNT and LC/*h*-BN interactions, and subsequently, this cell would exhibit a faster τ_{off} for the same cell thickness. On the other hand, the driving voltage is the dominating factor for $\tau_{on,}$ and therefore, the effect of the polar anchoring strength coefficient on τ_{on} is negligible [42,49]. We obtain $(\tau_{on}/d^2)_{PI\ cell}$ = 0.018 ms/μm^2 and $(\tau_{on}/d^2)_{VA\text{-}CNT/h\text{-}BN\ cell}$ = 0.015 ms/μm^2 —which is not a significant difference as expected.

The main purpose of this comparison is to demonstrate that the VA-CNT/*h*-BN HAN cell exhibited similar switching responses to that of a traditional HAN cell. We ran this dynamic electro-optic switching experiment for VA-CNT/*h*-BN HAN cell continuously for more than 24 hrs, and no significant change in the response was noticed.

III. CONCLUSION

We have experimentally demonstrated that the nanostructure-based VA-CNT/*h*-BN HAN cell can function like a traditional PI-based HAN cell. This cell showed the absence of a threshold voltage and exhibited the two characteristic times, τ_{on} and $\tau_{off,}$ for the field-induced dynamic response. These responses are within the comparable range of the traditional PI-based HAN cell. Thus, in a HAN device, the *inorganic* VA-CNT arrays and 2D *h*-BN can replace the conventional *organic* PI-alignment substrates when substitutes are necessary due to external factors. Realizing various LC-substrate interactions and then developing alternate LC alignment methods is essential for fundamental and applied research for LC-based electro-optic devices. This study advances the fundamental understanding of nanoscale manipulation of LCs and LC-orientation control using their interactions with nanostructured surfaces and then developing a nanostructure-based novel electro-optic HAN device for potential applications in various optical devices ranging from optical displays–to–smart windows–to–LC lenses.

Acknowledgments

This work was supported by the Office of Naval Research (N0001421WX01643; N0001421WX01108) and the USNA Research Office.

Figure Captions

FIG. 1: (a) and (b) SEM images of the top-view of VA-CNT arrays at two different length scales. Inset in (b): An SEM image of the side-view of VA-CNT arrays. The solid line is the vertical direction, and the dashed line is the average tilt of the CNT arrays. (c) A schematic illustration of LC-CNT interaction: anchoring of an LC molecule on the CNT surface due to π–π stacking by matching the LC's benzene rings on the CNT-honeycomb surface. The yellow ellipsoidal structure is a generic LC molecule, and the black cylindrical honeycomb structure is a CNT surface. A schematic representation of homeotropic LC alignment on VA-CNT arrays is shown. (d) and (e) Optical microscope images of a thin layer of LC on the VA-CNT arrays under parallel polarizers. (f) A microphotograph of a thin layer of LC on the VA-CNT arrays under the cross-polarized microscope. Inset in (f): An optical microscope image of a thin layer of unaligned LC on a glass substrate under crossed polarizers. The white bar in (f) represents 50 μm for the inset as well.

FIG. 2: (a) A schematic illustration of the planar alignment of nematic LC molecules (ellipsoids) on 2D *h*-BN (honeycomb structure). The LC's benzene rings are overlaying on the *h*-BN-honeycomb structure due to the epitaxial interaction between the LC and the *h*-BN lattice. (b) Raman shift of monolayer *h*-BN on copper foil. (c) A microphotograph of a thin layer of nematic LC E7 on the *h*-BN slide under the cross-polarized microscope where the director $\hat{n}$ is at 45^o with the crossed-polarizers. (d) A microphotograph of the same LC E7 on the *h*-BN slide when rotated by 45^o under the cross-polarized microscope.

FIG. 3: Optical transmission as a function wavelength for a standard PI on ITO coated glass slide, a monolayer *h*-BN on ITO coated glass slide, and VA-CNT arrays on Cr coated slide listed in the legend. The visible wavelength range is shown on the *x*-axis. The inset picture shows the VA-CNT /Cr quartz slide (left) and the *h*-BN/ITO glass slide (right).

FIG. 4: (a) A schematic representation of the VA-CNT/*h*-BN-based HAN cell. Two microphotographs the VA-CNT/*h*-BN-based HAN cell under the cross-polarized microscope where $\hat{n}$, at the *h*-BN side, is (b) at 45^o with the crossed polarizers, and (c) parallel to the analyzer. Two microphotographs of a traditional PI-based HAN cell for the two oriented states, (d) 45^o and (e) 0^o.

FIG. 5: (a) The transmittance (I/I_o) for the VA-CNT/*h*-BN-based HAN cell (at T = 22^o C) as a function of applied ac voltage (f = 1000 Hz) showing two maxima and the absence of a threshold voltage; top inset: the transmittance (I/I_o) for the traditional PI-based HAN cell (at T = 22^o C) as a function of applied AC voltage (f = 1000 Hz) showing one maximum and the absence of a threshold voltage; bottom inset: the transmittance (I/I_o) for the traditional PI-based planar cell (at T = 22^o C) as a function of applied ac voltage (f = 1000 Hz) showing three maxima and the presence

of a threshold voltage. Schematic representations of (b) voltage off and (c) voltage on states for the VA-CNT/*h*-BN-based HAN cell. (d) Seven separate microphotographs of the VA-CNT/*h*-BN-based HAN cell under the cross-polarized optical microscope at different applied voltages.

FIG. 6: Dynamics of electro-optic response for the (a) VA-CNT/*h*-BN-based HAN cell and the (b) the traditional PI-based HAN cell. The driving square wave voltage profile with f = 35 Hz is shown on the right-hand y-axis. The left-hand y-axis represents the normalized transmitted intensity as a function of time as the voltage is turned on and off (at T = 22^{o} C). The two characteristic times, τ_{on} and τ_{off}, are shown in (a).

References

1. S. Matsumoto, M. Kawamoto, and K. Mizunoya, "Field-induced deformation of hybrid-aligned nematic liquid crystals: New multicolor liquid crystal display", Journal of Applied Physics **47**(9), 3842-3845 (1976).
2. J.-J. P. Drolet, J. S. Patel, K.G. Haritos, W. Xu, A. Scherer, and D. Psaltis, "Hybrid-aligned nematic liquid-crystal modulators fabricated on VLSI circuits", Optics Letters **20**(21), 2222-2224 (1995).
3. C.C. Tartan, and S. J. Elston, "Hybrid aligned nematic based measurement of the sum (e_1+e_3) of the flexoelectric coefficients", J. Appl. Phys. **117**(6), 064107 (2015).
4. S. A. Jewell and J. R. Sambles, "Fully-leaky guided mode measurement of the flexoelectric constant (e11+e33) of a nematic liquid crystal", Mol. Cryst. Liq. Cryst., **401**(1) 67–73 (2003)
5. C. Kischka, S. J. Elston and E. P. Raynes, "Measurement of the Sum (e_1+e_3) of the Flexoelectric Coefficients e_1 and e_3 of Nematic Liquid Crystals using a Hybrid Aligned Nematic (HAN) cell", Molecular Crystals and Liquid Crystals, 494(1), 93–100 (2008).
6. A.J. Davidson and N.J. Mottram, "Flexoelectric switching in a bistable nematic device", Physical Eeview E **65**(5), 051710 (2002)
7. R.Yamaguchi and T. Takasu, "Hybrid aligned nematic liquid crystal smart glass with asymmetrical daylight controls", Journal of the Society for Information Display", **23**(8) 365-370 (2015).
8. T.-H. Choi, J.-W. Kim, and T.-H. Yoon, "Sub-Millisecond Switching of Hybrid-Aligned Nematic Liquid Crystals", Journal of Display Technology, **10**(12) 1088-1092 (2014).
9. C.-Y. Huang, Y.-J. Huang and Y.-H. Tseng, "Dual-operation-mode liquid crystal lens", Optics Express **17**(23) 20860–20865 (2009).
10. F. Yang, L. Ruan, S. A. Jewell and J. R. Sambles, "Polarization rotator using a hybrid aligned nematic liquid crystal cell", Optics Express 15(7) 4192-4197 (2007).
11. K. Takatoh, M. Hasegawa, M. Koden, N. Itoh, R. Hasegawa, and M. Sakamoto, *Alignment Technology and Applications of Liquid Crystal Devices* (Taylor & Francis, New York, 2005).
12. H.- S. Park and K.- C. Shin, "Liquid Crystal Cell Process" in *Flat Panel Display Manufacturing*, J. Souk, S. Morozumi, F.-C. Luo, and I. Bita, eds. (John Wiley & Sons, Ltd., West Sussex, 2018).
13. C.-H. Wen, S. Gauza, and S.-T. Wu, "Photostability of Liquid Crystals and Alignment Layers," J. Soc. Inf. Disp. **13**(9), 805−811 (2005).
14. Y.J. Lim, Y.E. Choi, S.-W. Kang, D.Y. Kim, S.H. Lee and Y.-B. Hahn, "Vertical alignment of liquid crystals with zinc oxide nanorods," Nanotechnology **24**(34), 345702 (2013).
15. J.-H. Kim and C. Rosenblatt, "Temperature effect on a rubbed polyimide alignment layer," J. Appl. Phys. **87**(1), 155-158 (2000).
16. N.A.J.M. Van Aerle, "Influence of polyimide orientation layer material on the liquid crystal resistivity in LCDs," Mol. Cryst. Liq. Cryst. **257**(1), 193-208 (1994).

17. R. Basu and S.A. Shalov, "Graphene as transmissive electrodes and aligning layers for liquid-crystal-based electro-optic devices," Phys. Rev. E **96**(1), 012702 (2017).
18. R. Basu and A. Lee, "Ion trapping by the graphene electrode in a graphene-ITO hybrid liquid crystal cell," Appl. Phys. Lett. **111**(16), 161905 (2017).
19. R. Basu and L.J. Atwood, "Characterizations of a Graphene-Polyimide Hybrid Electro-optical Liquid Crystal Device," OSA Continuum **2**(1), 83-91 (2019).
20. R. Basu, L.J. Atwood, "Two-dimensional hexagonal boron nitride nanosheet as the planar-alignment agent in a liquid crystal-based electro-optic device," Opt. Express **27**(1), 282-292 (2019).
21. R. Basu, L.J. Atwood, "Reduced ionic effect and accelerated electro-optic response in a 2D hexagonal boron nitride planar-alignment agent based liquid crystal device," Opt. Mater. Express **9**(3), 1441-1449 (2019).
22. R. Basu, "Enhancement of effective polar anchoring strength and accelerated electro-optic switching in a two-dimensional hexagonal boron nitride/polyimide hybrid liquid crystal device," Appl. Opt. **58**(24), 6678-6683 (2019).
23. R. Basu and L. Atwood, "Electro-optic liquid crystal device employing two-dimensional WSe_2 as the planar-alignment layers", Opt. Mater. Express **10**(6), 1405-1412 (2020).
24. M.-Z. Chen, S.-H. Yang, and S.-C. Jeng, "Growth of ZnO Nanorods and Their Applications for Liquid Crystal Devices," ACS Appl. Nano Mater. **1**(4), 1879−1885 (2018).
25. M.-Z. Chen, W.-S. Chen, S.-C. Jeng, S.-H. Yang, and Y.-F. Chung, "Liquid crystal alignment on zinc oxide nanowire arrays for LCDs applications," Opt. Express **21**(24) 29277-29282 (2013).
26. T. Maeda and K. Hiroshima, "Vertically aligned nematic liquid crystal on anodic porous alumina," Jpn. J. Appl. Phys. **43**(8A), L1004–L1006 (2004).
27. C. Hong, T.T. Tang, C.Y. Hung, R.P. Pan, and W. Fang, "Liquid crystal alignment in nanoporous anodic aluminum oxide layer for LCD panel applications," Nanotechnology **21**(28), 285201 (2010).
28. R. Basu and L.J. Atwood, "Homeotropic liquid crystal device employing vertically aligned carbon nanotube arrays as the alignment agent", Physical Review E **102**(2) , 022701 (2020).
29. www.nano-lab.com
30. R. Löffler, M. Häffner, G. Visanescu, H. Weigand, X. Wang, D. Zhang, M. Fleischer, A.J. Meixner, J. Fortágh, D.P. Kern, "Optimization of plasma-enhanced chemical vapor deposition parameters for the growth of individual vertical carbon nanotubes as field emitters," Carbon **49**(13), 4197-4203 (2011).
31. K.A. Park, S.M. Lee, S.H. Lee, and Y.H. Lee, "Anchoring a Liquid Crystal Molecule on a Single-Walled Carbon Nanotube," J. Phys. Chem. C **111**(4), 1620-1624 (2007).
32. M.D. Lynch and D.L. Patrick, "Organizing Carbon Nanotubes with Liquid Crystals," Nano Letters **2**(11), 1197-1201 (2002).
33. I. Dierking, G. Scalia, and P. Morales, "Liquid crystal–carbon nanotube dispersions," J. Appl. Phys. **97**(4), 044309 (2005).

34. R. Basu and G.S. Iannacchione, "Orientational coupling enhancement in a carbon nanotube dispersed liquid crystal," Phys. Rev. E **81**(5), 051705 (2010).
35. R. Basu and A. Garvey, "Insulator-to-conductor transition in liquid crystal-carbon nanotube nanocomposites," J. Appl. Phys. **120**(16), 164309 (2016).
36. R. Basu and G. S. Iannacchione, "Nematic anchoring on carbon nanotubes," Appl. Phys. Lett. **95**(17), 173113 (2009).
37. R. Basu, K. Boccuzzi, S. Ferjani and C. Rosenblatt; "Carbon nanotube induced chirality in an achiral liquid crystal," Appl. Phys. Lett. **97**(12), 121908 (2010)
38. R. Basu, R. G. Petschek and C. Rosenblatt, "Nematic electroclinic effect in a carbon nanotube doped achiral liquid crystal," Phys. Rev. E **83**(4), 041707 (2011).
39. P. Kalakonda, R. Basu, I. R. Nemitz, C. Rosenblatt, and G. S. Iannacchione, "Studies of nanocomposites of carbon nanotubes and a negative dielectric anisotropy liquid crystal," J. Chem. Phys. **140**(10), 104908 (2014).
40. R. Basu, C.-L. Chen, and C. Rosenblatt, "Carbon nanotube-induced macroscopic helical twist in an achiral nematic liquid crystal," J. Appl. Phys. **109**(8), 083518 (2011).
41. R. Basu, C. Rosenblatt, and R. Lemieux; "Chiral induction in thioester and oxoester liquid crystals by dispersed carbon nanotubes," Liq. Cryst. **39**(2), 199 (2012).
42. Y. Lu and L. C. Chien, "Carbon nanotube doped liquid crystal OCB cells: physical and electro-optical properties," Opt. Express **16**(17) , 12777–12785 (2008).
43. M.A. Shehzad, D.H. Tien, M.W. Iqbal, J. Eom, J.H. Park, C. Hwang, Y. Seo, "Nematic liquid crystal on a two dimensional hexagonal lattice and its application," Sci. Rep. **5**, 13331 (2015).
44. R. V. Gorbachev, I. Riaz, R. R. Nair, R. Jalil, L. Britnell, B. D. Belle, E. W. Hill, K. S. Novoselov, K. Watanabe, T. Taniguchi, A. K. Geim, and P. Blake "Hunting for Monolayer Boron Nitride: Optical and Raman Signatures," Small **7**(4), 465-468 (2011).
45. X. Li, Y. Zhu, W. Cai, M. Borysiak, B. Han, D. Chen, R. D. Piner, L. Colombo, and R. S. Ruoff, "Transfer of Large-Area Graphene Films for High-Performance Transparent Conductive Electrodes," Nano Lett. **9**(12), 4359–4363 (2009).
46. X. Liang, B.A. Sperling, I. Calizo, G. Cheng, C. A. Hacker, Q. Zhang, Y. Obeng, K. Yan, H. Peng, Q. Li, X. Zhu, H. Yuan, A.R.H. Walker, Z. Liu, L.-M. Peng, and C.A. Richter, "Toward clean and crackless transfer of graphene," ACS Nano **5**(11), 9144–9153 (2011).
47. D.S. Ghosh, L. Martinez, S. Giurgola, P. Vergani, and V. Pruneri, "Widely transparent electrodes based on ultrathin metals," Opt. Lett. **34**(3), 325-327 (2009).
48. L.M. Blinov and V.G. Chigrinov, *Electro-optic Effects in Liquid Crystal Materials* (Springer-Verlag, New York, 1996).
49. X. Nie, R. Lu, H. Xianyu, T. X. Wu, and S. T. Wu, "Anchoring energy and cell gap effects on liquid crystal response time," J. Appl. Phys. **101**(10), 103110 (2007).
50. R. Basu, "Enhancement of polar anchoring strength in a graphene-nematic suspension and its effect on nematic electro-optic switching," Physical Review E **96**(1), 012707 (2017).

Fig. 1

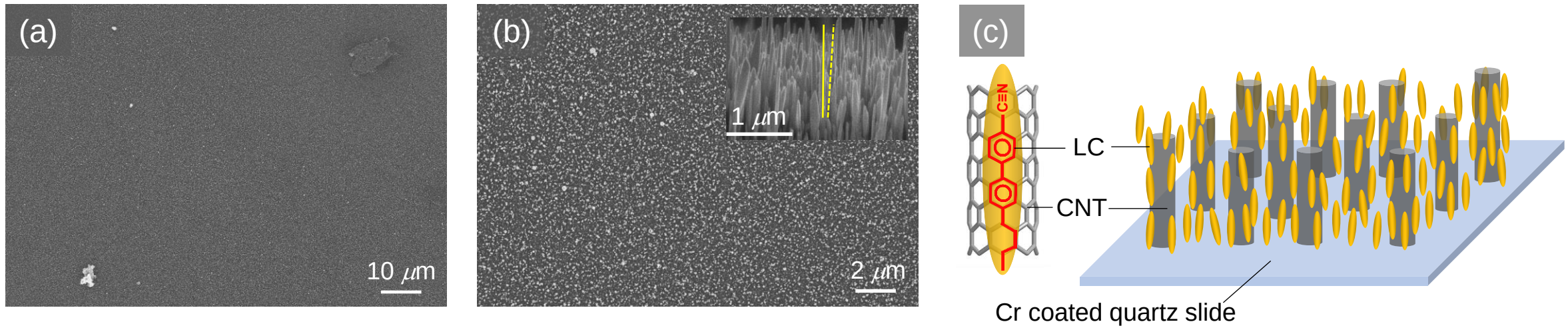
(a)
10 μm
(b)
1 μm
2 μm
(c)
C≡N
LC
CNT
Cr coated quartz slide
(d)
AP
LC on VA-CNTs
Bare VA-CNTs
50 μm
(e)
AP
LC on VA-CNTs
50 μm
(f)
A
P
50 μm

Fig. 2

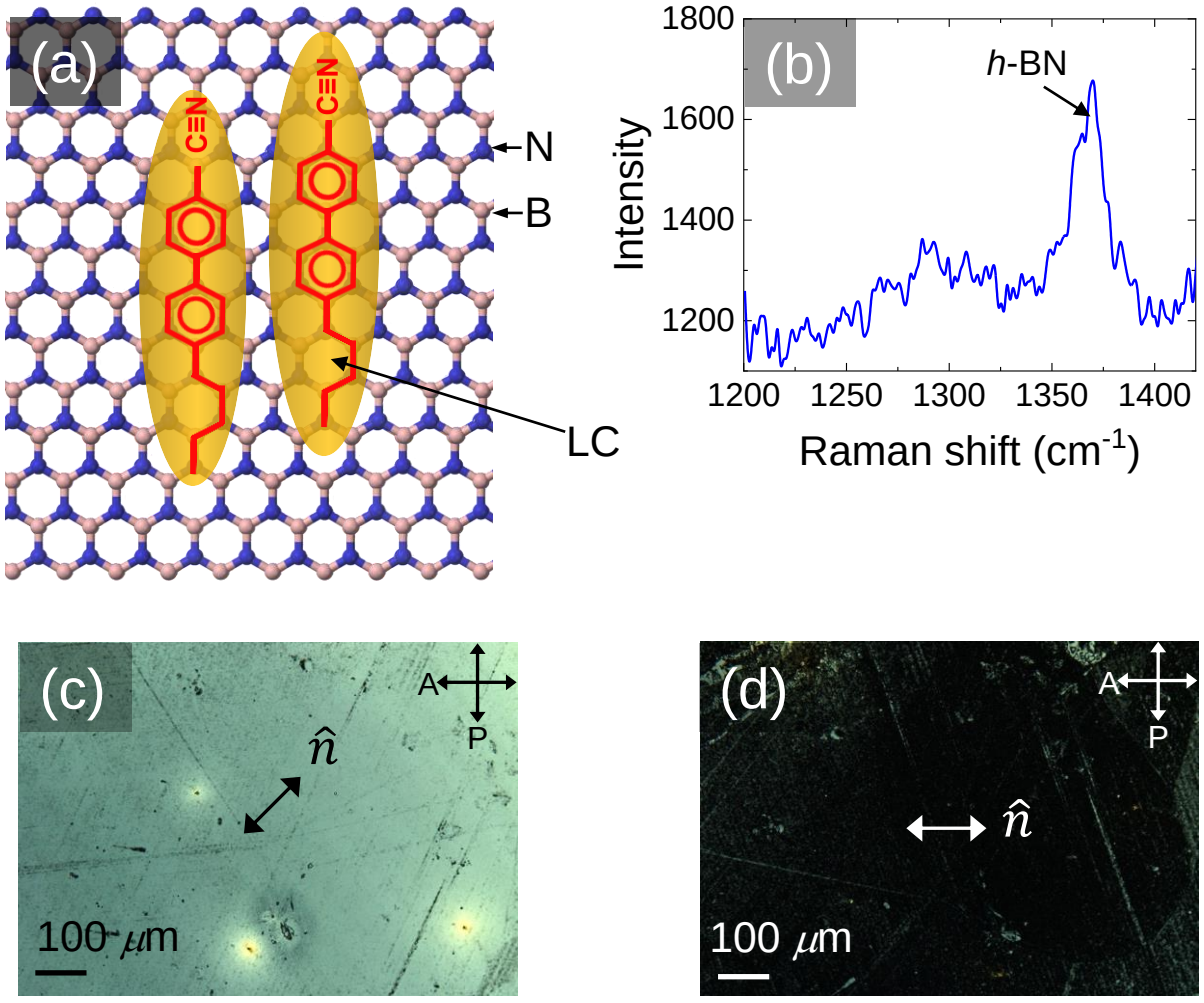
(a)
C≡N
C≡N
N
B
LC
(b)
h-BN
Intensity
1800
1600
1400
1200
1200
1250
1300
1350
1400
Raman shift (cm-1)
(c)
A
P
n̂
100 μm
(d)
A
P
n̂
100 μm

Fig. 3

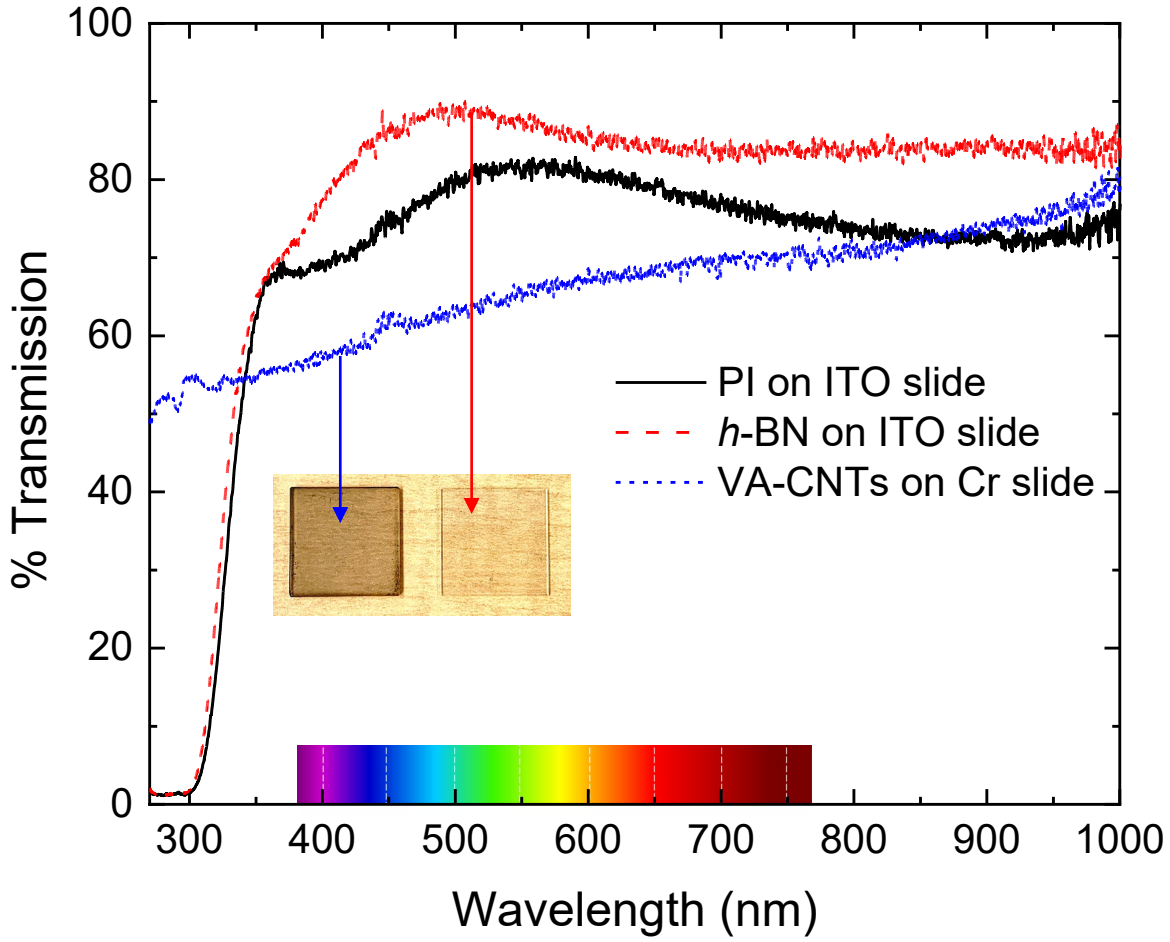
100
80
60
40
20
0
% Transmission
300
400
500
600
700
800
900
1000
Wavelength (nm)
PI on ITO slide
h-BN on ITO slide
VA-CNTs on Cr slide

Fig. 4

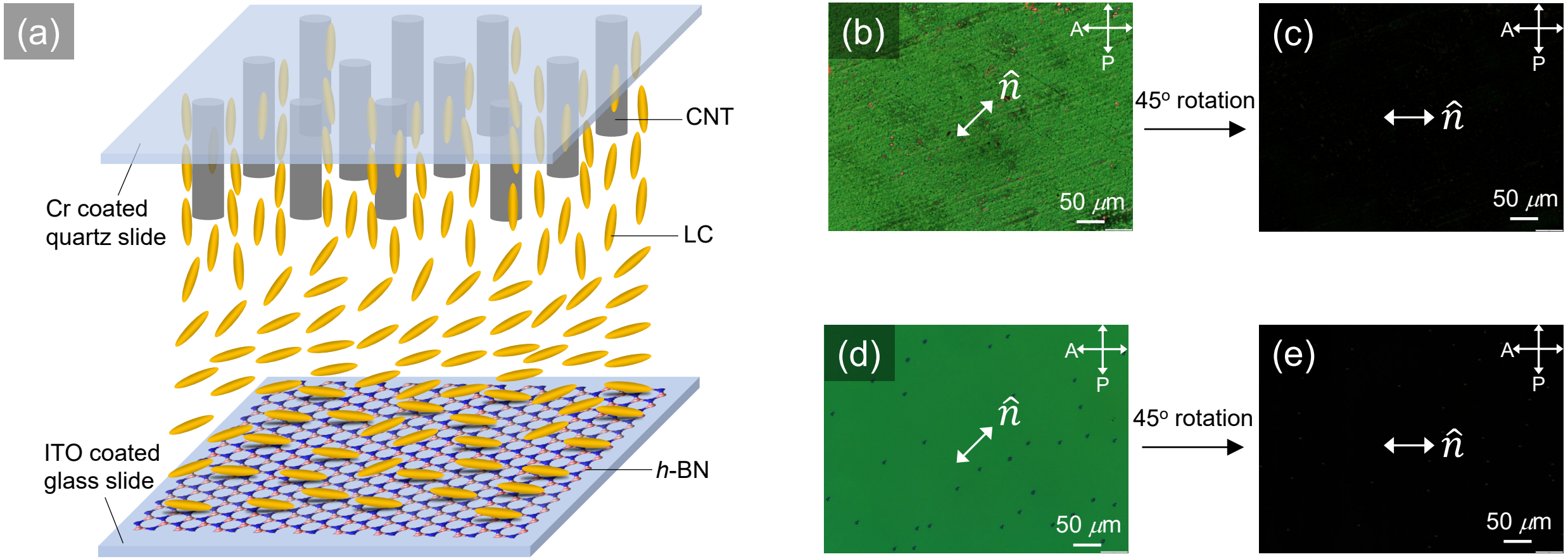
(a)
CNT
Cr coated
quartz slide
LC
ITO coated
glass slide
h-BN
(b)
A
P
$\hat{n}$
50 μm
45° rotation
(c)
A
P
$\hat{n}$
50 μm
(d)
A
P
$\hat{n}$
50 μm
45° rotation
(e)
A
P
$\hat{n}$
50 μm

Fig. 5

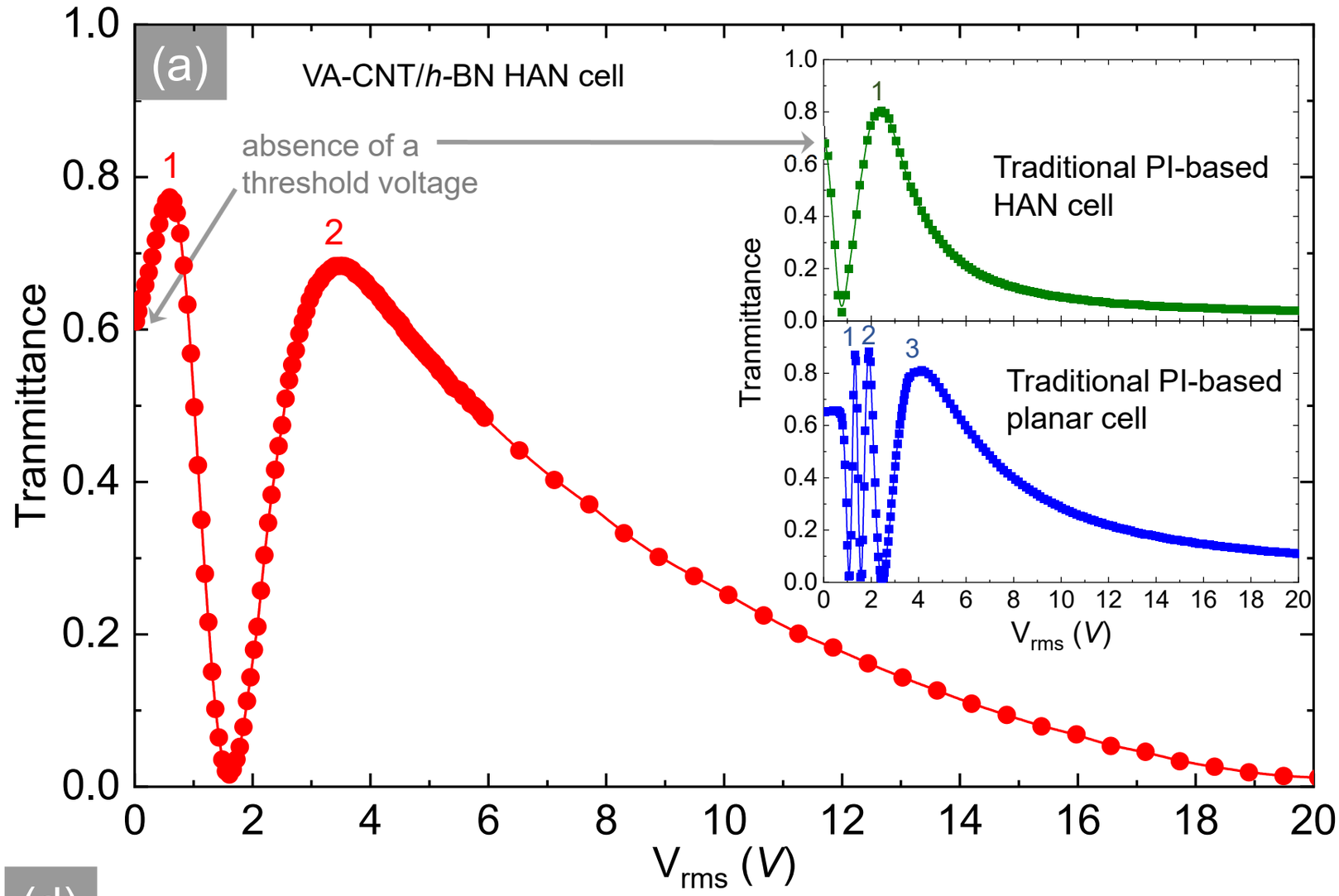
(a)
VA-CNT/h-BN HAN cell
absence of a
threshold voltage
1
2
Tranmittance
1.0
0.8
0.6
0.4
0.2
0.0
0
2
4
6
8
10
12
14
16
18
20
V_rms (V)
Traditional PI-based
HAN cell
1
Traditional PI-based
planar cell
1 2
3
Tranmittance
V_rms (V)

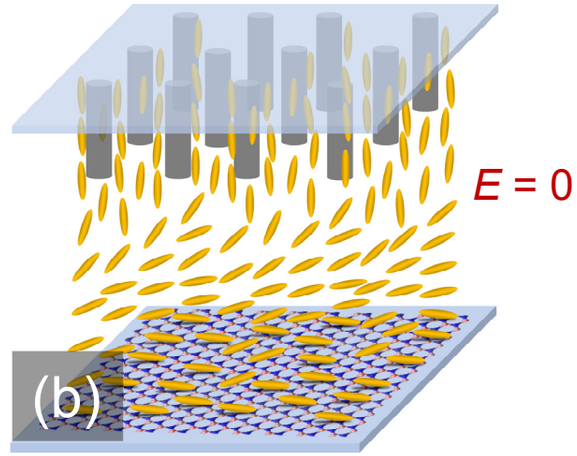
(b)
E = 0

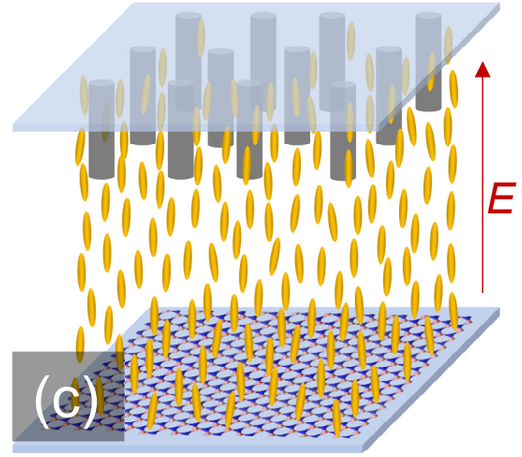
(c)
E

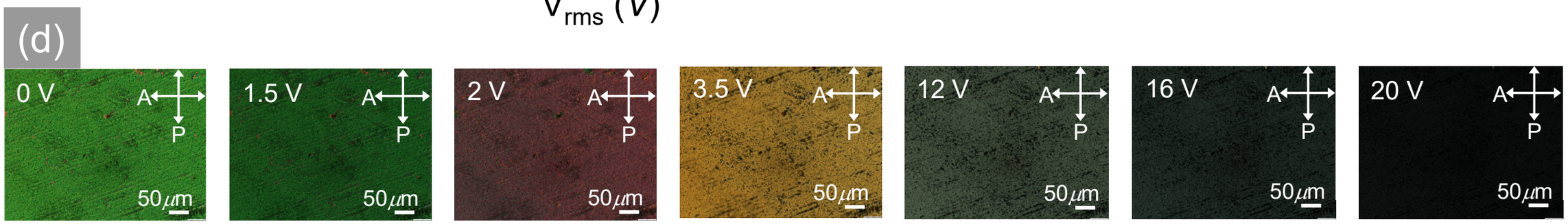
(d)
0 V
1.5 V
2 V
3.5 V
12 V
16 V
20 V
A
P
50μm

Fig. 6

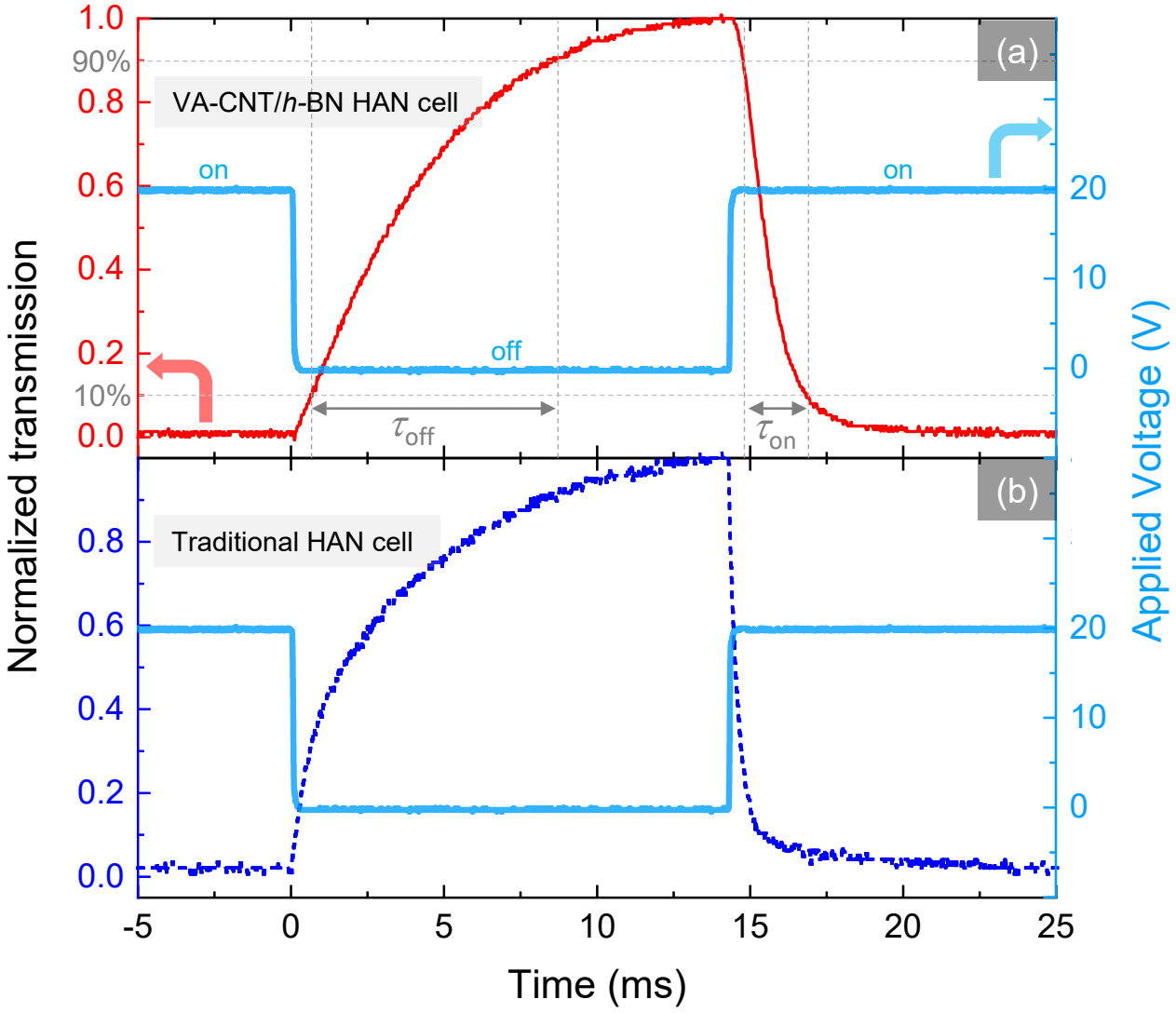
(a)
VA-CNT/h-BN HAN cell
on
off
on
90%
10%
τ_{off}
τ_{on}
(b)
Traditional HAN cell
Normalized transmission
Applied Voltage (V)
Time (ms)
1.0
0.8
0.6
0.4
0.2
0.0
20
10
0
-5
0
5
10
15
20
25